Journal of Power Sources 375 (2018) 106–117

Contents lists available at ScienceDirect

Journal of Power Sources

journal homepage: www.elsevier.com/locate/jpowsour

Modeling the degradation mechanisms of C_6/$LiFePO_4$ batteries

Dongjiang Li[a], Dmitri L. Danilov[a,b], Barbara Zwikirsch[c], Maximilian Fichtner[c], Yong Yang[d], Rüdiger-A. Eichel[a,e], Peter H.L. Notten[a,b,f,*]

[a] Forschungszentrum Jülich, Fundamental Electrochemistry (IEK-9), D-52425, Jülich, Germany
[b] Department of Electrical Engineering, Eindhoven University of Technology, Eindhoven, 5600 MB, The Netherlands
[c] Helmholtz Institute Ulm for Electrochemical Energy Storage (HIU), D-89081, Ulm, Germany
[d] State Key Lab for Physical Chemistry of Solid Surfaces, Department of Chemistry, Xiamen University, Xiamen, 361005, China
[e] RWTH Aachen University, D-52074, Aachen, Germany
[f] Department of Chemical Engineering and Chemistry, Eindhoven University of Technology, Eindhoven, 5600 MB, The Netherlands

HIGHLIGHTS

- Capacity losses of C_6/$LiFePO_4$ batteries are investigated under storage and cycling.
- SEI formation is the main reason for capacity loss at moderate temperatures (≤ 40°C).
- Cathode dissolution at elevated temperatures (>40°C) accelerates capacity loss.
- SEI formation model and cathode dissolution model are developed.

ARTICLE INFO

Keywords:
Li-ion batteries
Modeling
Solid-Electrolyte-Interface
Capacity fade
Material decay

ABSTRACT

A fundamental electrochemical model is developed, describing the capacity fade of C_6/$LiFePO_4$ batteries as a function of calendar time and cycling conditions. At moderate temperatures the capacity losses are mainly attributed to Li immobilization in Solid-Electrolyte-Interface (SEI) layers at the anode surface. The SEI formation model presumes the availability of an outer and inner SEI layers. Electron tunneling through the inner SEI layer is regarded as the rate-determining step. The model also includes high temperature degradation. At elevated temperatures, iron dissolution from the positive electrode and the subsequent metal sedimentation on the negative electrode influence the capacity loss. The SEI formation on the metal-covered graphite surface is faster than the conventional SEI formation. The model predicts that capacity fade during storage is lower than during cycling due to the generation of SEI cracks induced by the volumetric changes during (dis)charging. The model has been validated by cycling and calendar aging experiments and shows that the capacity loss during storage depends on the storage time, the State-of-Charge (SoC), and temperature. The capacity losses during cycling depend on the cycling current, cycling time, temperature and cycle number. All these dependencies can be explained by the single model presented in this paper.

1. Introduction

Ageing has become an important research topic since batteries are widely applied in portable electronic devices, electric vehicles and smart grid energy storage, *etc*. Long calendar and cycle life are critical for Li-ion batteries in these applications [1,2]. Understanding the aging mechanisms is essential for improving the life-span of Li-ion batteries.

The SEI formation and electrode material degradation are considered to be the main reasons for battery aging. It has been unraveled that the SEI formation on the anode is the major cause of battery capacity losses [3–9]. Considerable efforts have been made to study the structural and chemical composition of SEI layers [10–20]. It has been found that the SEI affects the performance of Li-ion batteries in two different ways. On the one hand, it immobilizes cyclable lithium in the battery, which is therefore no longer available for the energy storage and, subsequently, leads to irreversible capacity losses. On the other hand, it protects the anode surface from solvent co-intercalation, preventing exfoliation of the graphene sheets. Experimental studies demonstrate that the SEI is composed of a thin inner SEI layer and a more porous and extended outer SEI layer [10–12]. The inner SEI-layer is dense and prevents the surface of the anode from direct contact with the electrolyte, thereby suppressing co-intercalation of the solvent. The

* Corresponding author. Forschungszentrum Jülich, Fundamental Electrochemistry (IEK-9), D-52425, Jülich, Germany.
E-mail address: p.h.l.notten@tue.nl (P.H.L. Notten).

https://doi.org/10.1016/j.jpowsour.2017.11.049
Received 13 September 2017; Received in revised form 10 November 2017; Accepted 16 November 2017
Available online 24 November 2017
0378-7753/

inner layer of SEI is good Li^+ ionic conductor. The outer SEI layer, on the other hand, is porous, enabling fast transport of solvated Li^+ ions.

Although considerable efforts were made to study the SEI experimentally, the understanding of lithium immobilization is still limited due to the complexity of the SEI formation reaction, which was found to be highly dependent on the electrode voltage, electrode surface morphology and the composition of the electrolyte. Modeling is a powerful tool to study the SEI formation process. However, only a limited number of studies refer to the SEI growth process, which are still under discussion [6–9,21–31]. Some authors assumed the electron tunneling process to be rate-determining for SEI formation [5,6,24,30] while others regarded solvent diffusion through the SEI layer as a rate-limiting step [27–29].

Apart from the SEI formation, cathode dissolution at elevated temperatures is considered to be another important process during battery aging [7,9,32–35]. The dissolved transition metal ions can be transported to the anode and can subsequently be deposited on the graphite surface [7,9]. Both the metal dissolution and the subsequent reduction can directly lead to a decrease of the battery capacity. Furthermore, the deposited metal clusters will speed up the SEI development by facilitating the transport of electrons [7,9,32].

An electrochemical model has been developed in our previous work in order to simulate the SEI growth at room temperature [5,6]. In the present work we extended the SEI formation model to various cycling currents, storage at different SoC and temperatures. Apart from the SEI formation, the cathode dissolution and Fe plating at anode at elevated temperatures will also be modeled in the present work. The model has been validated by experimental data. Good agreement between simulations and experiments is found in all cases.

2. Model development

Cyclable Li^+ ions and electrons are originally stored in the $LiFePO_4$ electrode in $C_6/LiFePO_4$ (LFP) batteries after manufacturing. The maximum battery capacity (Q^0_{max}) therefore equals to the total amount of cyclable Li^+ ions in the cathode materials ($Q^0_{LiFePO_4}$). During charging (ch) electrons are extracted from the $LiFePO_4$ electrode and flow into the graphite electrode via the outer circuit. Simultaneously, Li^+ ions are transported from the $LiFePO_4$ electrode via the electrolyte to the graphite electrode to safeguard the system electro-neutrality. The reverse reactions take place during discharging (d). The main electrochemical storage reactions of LFP batteries can be described by Ref. [6].

$$C_6 + Li^+ + e^- \underset{d}{\overset{ch}{\rightleftarrows}} LiC_6 \quad (1)$$

$$LiFePO_4 \underset{d}{\overset{ch}{\rightleftarrows}} FePO_4 + Li^+ + e^- \quad (2)$$

Electrons extracted from the lithium iron-phosphate electrode can also be partially consumed by many processes, such as parasitic side reactions taking place at the graphite electrode during cycling and storage, leading to irreversible capacity losses. The detailed capacity loss mechanisms during cycling and storage will be discussed in the following sections.

2.1. The SEI formation model

The formation mechanisms and composition of SEI layers have been widely investigated. Although there are still some debates, it has been generally accepted that the SEI layers are composed of inorganic and organic Li salts, and constitute the dense inner layer and porous outer layer, respectively, as schematically shown in Fig. 1. The inner SEI layer is an electronic insulator. It also prevents solvents from passing through and co-intercalating into the graphene layers. Therefore, it is assumed, that solvent reduction takes place at the interface between the inner and outer SEI layers.

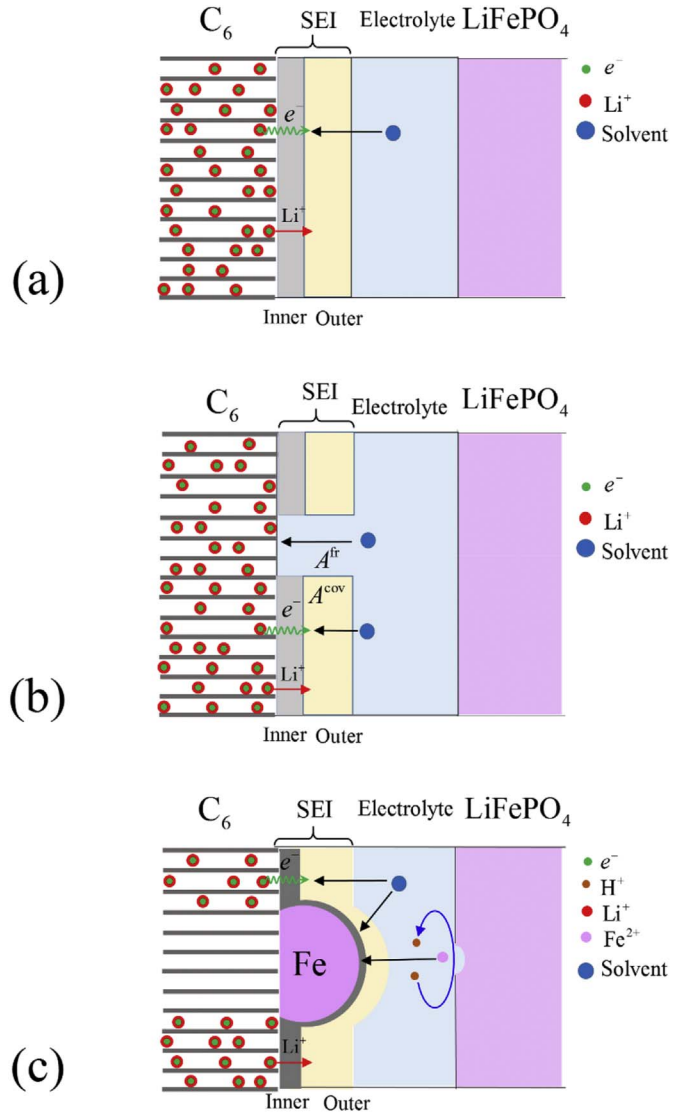

Fig. 1. Schematic representation of SEI formation on the graphite electrode inside a LFP battery under storage (a) and cycling (b) conditions. (c) The influence of elevated temperatures on aging processes inside LFP batteries [7,9].

Electrons at the graphite electrode surface can, however, tunnel across the inner SEI layer to the Lowest Unoccupied Molecular Orbital (LUMO) of the solvent. Literature reports several values for the Fermi level of metallic Li and LiC_6 [36–38]. In the present work we adopt the results reported by Wertheim et al. [38], namely −2.36 eV for Li and −2.80 eV for LiC_6 *vs* vacuum. For Ethylene Carbonate (EC) in the presence of Li^+ ions the LUMO was found to be −2.99 eV [6]. This value is below the Fermi level of the lithiated graphite and, therefore, EC will be reduced, presuming that electrons can pass the energy barrier by tunneling.

The SEI development starts when the voltage of the negative electrode declines below 1.0 V *vs* Li^+/Li [12,15,17]. Therefore, the SEI is developed during the activation procedure immediately after the end of battery manufacturing process. The quality of the SEI formed during this activation process determines the battery cycling performance in their application. An ideal SEI layer formed during the activation procedure can dramatically decrease the further SEI formation rate and, therefore, maintain a high battery coulombic efficiency. However, in practice the SEI layers continue to grow during battery operation, leading to continuous irreversible capacity losses.

During (dis)charging, Li^+ ions can readily penetrate both the inner

and outer SEI layers. Solvent molecules, in contrast, can readily pass the porous outer SEI layer but cannot penetrate the inner SEI layer [6]. The inner SEI layer is a good electronic insulator but electrons can tunnel through it when its thickness is sufficiently small (< 3 nm). The electron tunneling process is regarded as rate-determining. The products of these reduction reactions increase the thickness of both SEI layers but the individual formation rates might significantly differ as will be shown below.

Fig. 1a schematically shows the SEI formation process in the case of storage. Under open-circuit conditions there is no current flow through the outer circuit, therefore no significant volume changes of the graphite electrode occur during storage. When a battery is stored at a predetermined State-of-Charge (SoC), electrons from the graphite electrode surface can freely tunnel across the inner layer and, subsequently, reduce the solvent molecules at the inner/outer SEI interface. Obviously, this reduction reaction should be counter-balanced under open-circuit conditions by an oxidation reaction as no external current is flowing. Oxidation of lithium stored inside the graphite electrode will simultaneously take place at the graphite/inner SEI layer interface. The liberated Li^+ ions further diffuse through the inner SEI layer into the electrolyte. This electron tunneling process combined with Li^+ ions leaving the electrode ultimately results in Li-immobilization in the SEI layers and hences irreversible capacity losses even under open-circuit conditions.

When electron tunneling is considered to be the rate determining step, the Li consumption rate in both the inner and outer SEI layers during storage has been described [5,6] by the following Ordinary Differential Equation (ODE)

$$\frac{dQ_{SEI}^{st}(t)}{dt} = \frac{(6+x)F\rho_{C_6}v_eA_{C_6}}{4M_{C_6}}P_0\exp\left(-\frac{2\left(l_0^{in}+\frac{M_{Li}\delta_{C_6}Q_{SEI}^{st}(t)}{\rho^{in}A_{C_6}w_{Li}^{in}F}\right)\sqrt{2m\Delta E}}{\hbar}\right) \tag{3}$$

where $Q_{SEI}^{st}(t)$ is the charge related to the amount of immobilized Li^+ [C] in both outer and inner SEI layers during storage from $t = 0$ up to t, multiplier 6 indicates the number of free electrons per each C_6 molecule, x is the SoC of the anode ($0 \le x \le 1$), F is the Faraday constant [C·mol^{-1}], ρ_{C_6} the gravimetric density of graphite [g·m^{-3}], v_e the Fermi velocity of electrons in graphite [m·s^{-1}], A_{C_6} the active surface area of the anode [m^2], M_{C_6} the molar mass of graphite [g·mol^{-1}], factor 4 in the denominator results from the assumption that the direction of electronic velocity within the layer of graphene takes one of four orthogonal directions with equal probabilities (1/4). P_0 is the pre-exponential coefficient, which is considered to be unity in the present work. l_0^{in} defines the initial thickness of inner SEI layer immediately after the activation process. Parameter l_0^{in} depends on the activation conditions and found to be around 2.0 nm [39]. M_{Li} is the molar mass of metallic Li [g·mol^{-1}], ρ^{in} the (average) gravimetric density of the inner SEI layer [g·m^{-3}], w_{Li}^{in} the average weight fraction of lithium in the SEI inner layer (dimensionless) and δ_{C_6} is the ratio between the capacity losses related to the inner SEI layer, and to the total SEI layer ($Q_{SEI}(t)$) at the graphite electrode surface. δ_{C_6} is dependent on the aging conditions. $\hbar$ is the reduced Planck constant, m the electron mass [g] and ΔE is the electron tunneling barrier [J].

Fig. 1b schematically shows the SEI formation process in case of cycling. It is commonly accepted that the process of SEI formation can be significantly influenced by the volumetric shrinkage/expansion of anodes during (dis)charging [7,8,40,41]. These volumetric changes result in mechanical stress, creating cracks in the SEI layers and therefore inducing the formation of uncovered graphite surface (A^{fr}). As a result, the solvent is directly brought in contact with pristine graphite and will immediately be reduced, leading to new SEI products. Therefore, these volumetric changes have a significant impact on the increased capacity losses during cycling.

In the case of cycling, cracks in the SEI layers will be systematically produced when the volume of the graphite particles increases during charging. Therefore, the SEI formation will continue on the SEI covered surface A^{cov} which leads to a capacity loss $Q_{SEI}^{cov}(t)$ but will also occur at the freshly formed cracks (A^{fr}), which leads to a capacity loss Q_{SEI}^{fr}. The SEI formation on A^{cov} can then be described by Ref. [6].

$$\frac{dQ_{SEI}^{cov}(t)}{dt} = \frac{(6+0.5)F\rho_{C_6}v_eA^{cov}}{4M_{C_6}}P_0\exp\left(-\frac{2\left(l_0^{in}+\frac{M_{Li}\delta_{C_6}Q_{SEI}^{cov}(t)}{\rho^{in}A^{cov}w_{Li}^{in}F}\right)\sqrt{2m\Delta E}}{\hbar}\right) \tag{4}$$

where $Q_{SEI}^{cov}(t)$ is the capacity loss due to the SEI formation at the covered surface. To simplify this equation a 50% State-of-Charge is assumed, *i.e.* $x = 0.5$, and $\overline{\Delta E(t)} = \Delta E$.

When SEI is built at the fresh surface, the inner layer of SEI develops from 0 to l_{fr}^{in} at the i^{th} cycle. This SEI formation rate can be written as

$$\frac{dQ_{SEI}^{fr}(t_i)}{dt_i} = \frac{(6+0.5)F\rho_{C_6}v_eA^{fr}}{4M_{C_6}}P_0\exp\left(-\frac{2M_{Li}\delta_{C_6}Q_{SEI}^{fr}(t_i)\sqrt{2m\Delta E}}{\rho^{in}A^{fr}w_{Li}^{in}F\hbar}\right) \tag{5}$$

Note that time t_i in Eq. (5) refers to the duration of the i^{th} cycle. Considering that all cycles are full (dis)charge cycles this differential equation remains the same for all cycles, thus $Q_{SEI}^{fr}(t_i)$ can be considered constant (χ) when t_i does not change too much, *i.e.*

$$Q_{SEI}^{fr} = \chi \tag{6}$$

The total capacity loss caused by the crack formation during the whole cycling process can be written as

$$Q_{SEI}^{cr} = \sum_{i=1}^{n} Q_{SEI}^{fr}(i) = n\chi \tag{7}$$

where n refers to the number of full (dis)charge cycles.

2.2. Cathode dissolution model

At elevated temperatures other degradation processes may take place, such as cathode dissolution, electrolyte decomposition, graphite deformation, *etc*. Among these processes, cathode dissolution has the most significant impact [32]. It has been shown that transition metal ions can be exchanged by protons in the electrolyte [34]. These protons originate from water traces in the electrolyte, according to

$$Li^+ + PF_6^- \xrightarrow{\text{elevated T}} LiF + PF_5 \tag{8}$$

$$PF_5 + H_2O \rightarrow 2H^+ + 2F^- + POF_3 \tag{9}$$

It can be concluded from Eqs. (8) and (9) that both the temperature and water content are essential conditions to produce protons in the electrolyte.

Fig. 1c schematically shows the influence of the cathode dissolution process on the SEI formation. Fe^{2+} ions dissolve from the positive electrode by proton exchange with the electrolyte. The Fe^{2+} ions are then subsequently transported to the anode and reduced at the graphite surface. XPS analyses have confirmed that the deposited metal clusters are embedded inside the SEI layers [7,9]. These metal particles strongly accelerate the SEI formation since electron transport will be highly facilitated by these metallic iron particles. Therefore, more severe capacity degradation may be expected at the elevated temperatures.

2.2.1. Iron dissolution at the cathode

For simplicity reasons the iron ions dissolved from the cathode are assumed to be in the divalent Fe^{2+} state only. The dissolution of Fe^{2+} can be represented by the following protons exchange reaction

$$2H^+ + LiFePO_4 \xrightarrow{\widetilde{K}_e} Fe^{2+} + LiH_2PO_4 \tag{10}$$

The formed LiH_2PO_4 will further dissociate and dissolve into the

electrolyte, according to

$$LiH_2PO_4 \xrightarrow{\tilde{K}_d} 2H^+ + Li^+ + PO_4^{3-} \quad (11)$$

where $\tilde{k}_e$ and $\tilde{k}_d$ represent the rate constants of the exchange and dissociation reactions, respectively. $\tilde{k}_d$ is expected to be much larger than $\tilde{k}_e$, therefore the exchange reaction (Eq. (10)) is considered to be rate-determining. $\tilde{k}_e$ is temperature dependent, according to

$$\tilde{k}_e = k_e^0 \exp\left(-\frac{E_a^e}{RT}\right) \quad (12)$$

where k_e^0 is the pre-exponential factor and E_a^e is the activation energy [J·mol^{-1}]. Combining Eqs. (10) and (11), it can be concluded that the H^+ ions are continuously regenerated by the exchange and dissociation process. Consequently, the total concentration of H^+ ions in the electrolyte will not be influenced by the above processes and c_{H^+} [mol·m^{-3}] can therefore be considered constant. The dissolution flux of Fe^{2+} from the cathode $J^c_{Fe^{2+}}$, [mol·s^{-1}·m^{-2}] is obtained from Eq. (10), according to

$$J^c_{Fe^{2+}} = A_{LiFePO_4}\tilde{k}_e a^2_{H^+} a_{LiFePO_4} \quad (13)$$

where A_{LiFePO_4} is the surface area of the cathode [m^2], a_{H^+} is the activity of H^+ in the electrolyte ($a_{H^+} = c_{H^+}$) and a_{LiFePO_4} is the activity of the cathode material. Assuming that A_{LiFePO_4} is more or less constant during cycling and storage, $A_{LiFePO_4}\tilde{k}_e$ can be combined into k_e. When furthermore the activity of the solid $LiFePO_4$ is considered unity, Eq. (13) can be simplified to

$$J^c_{Fe^{2+}} = k_e c^2_{H^+} \quad (14)$$

2.2.2. Iron reduction at the anode

Fe^{2+} ions will be transported to the graphite electrode and, subsequently, be deposited at the graphite surface. The reduction reaction of Fe^{2+} ions can be represented by

$$Fe^{2+} + 2e^- \xrightarrow{k} Fe \quad (15)$$

where k is the Fe^{2+} charge-transfer constant. To maintain charge neutrality at the graphite electrode, two cyclable Li^+ ions per Fe^{2+} ion must be transported from the electrode to the electrolyte, and two electrons become available for iron reduction, according to

$$2LiC_6 \rightarrow 2C_6 + 2e^- + 2Li^+ \quad (16)$$

Fe^{2+} reduction at the graphite electrode is an electrochemical process which can in principle be described by the Butler-Volmer equation. However, the standard redox potential of Fe^{2+}/Fe is approximately 2.6 V *vs* Li^+/Li, which is much higher than the electrode potential of Li_xC_6, indicating that the overpotential of the Fe^{2+} reduction reaction (Eq. (15)) is very high. Considering the low Fe^{2+} concentration in the electrolyte, it can therefore be assumed that Fe^{2+} reduction at the graphite electrode is diffusion-controlled.

Considering steady state $\left(\frac{\partial c_{Fe^{2+}}}{\partial t} = 0\right)$, the reduction flux of Fe^{2+} ions at the anode ($J^a_{Fe^{2+}}$) must be equal to the dissolution flux given by Eq. (14), *i.e.*

$$J^a_{Fe^{2+}} = J^c_{Fe^{2+}} = k_e c^2_{H^+} \quad (17)$$

Using Eq. (17) the total molar amount of deposited Fe (N_{Fe}) can be determined, according to

$$N_{Fe} = \int_0^t J^a_{Fe^{2+}} dt = k_e c^2_{H^+} t \quad (18)$$

2.2.3. Iron-induced Li losses

Cyclable Li^+ ions are simultaneously released into the electrolyte from the cathode material during iron dissolution, according to Eqs. (10) and (11). The flux of Li^+ ions released at the cathode is equal to the flux of dissoluted Fe,

$$J^c_{Li^+} = J^c_{Fe^{2+}} = k_e c^2_{H^+} \quad (19)$$

It has been concluded from Eqs. (15) and (16) that after the reduction of each Fe^{2+} ion, two cyclable Li^+ ions will be released. Therefore, the flux of Li^+ ions oxidized at the anode is twice the Fe^{2+} reduction flux

$$J^a_{Li^+} = 2J^a_{Fe^{2+}} = 2k_e c^2_{H^+} \quad (20)$$

The battery capacity loss caused by Fe dissolution and reduction can therefore be obtained from

$$Q_{Li,Fe} = F\int_0^t (J^a_{Li^+} + J^c_{Li^+})dt = 3Fk_e c^2_{H^+} t \quad (21)$$

2.2.4. Fe-induced SEI formation

The iron clusters deposited on the graphite surface can facilitate the SEI development by improving electron transport. To simplify derivations, the iron particles deposited on the graphite surface are assumed to be semi-spherical and all semi-spherical iron clusters have the same size with radius r. The total volume of iron particles V_{Fe} [m^3] can then be written as

$$V_{Fe} = \frac{2\pi N r^3}{3} \quad (22)$$

where N is a constant, representing the total numbers of the Fe clusters. The volume of the Fe particles can be represented by

$$V_{Fe} = \frac{N_{Fe}M_{Fe}}{\rho_{Fe}} \quad (23)$$

where ρ_{Fe} is the density of Fe [g·m^{-3}] and M_{Fe} is the molar mass of Fe [g·mol^{-1}]. r can be obtained by combining Eqs. (22) and (23)

$$r = \left(\frac{3N_{Fe}M_{Fe}}{2\pi N\rho_{Fe}}\right)^{1/3} \quad (24)$$

The surface area available for enhanced SEI formation at Fe is

$$A_{Fe} = 2\pi N\left(\frac{3N_{Fe}M_{Fe}}{2\pi N\rho_{Fe}}\right)^{2/3} \quad (25)$$

Considering Eq. (18), the dependence of A_{Fe} can be represented as a function of time t by

$$A_{Fe} = 2\pi N\left(\frac{3k_e c^2_{H^+} M_{Fe} t}{2\pi N\rho_{Fe}}\right)^{2/3} \quad (26)$$

Similar to the lithium immobilization on the graphite surface, the SEI development on Fe can be described by the electron tunneling model since solvent molecules are reduced at the surface of iron in the same way as at the surface of graphite. The rate of the SEI formation on Fe surface can be written as

$$\frac{dQ_{SEI,Fe}(t)}{dt} = \frac{F\rho_{Fe}u_e A_{Fe}}{M_{Fe}}P_0 \exp\left(-\frac{2(l^0_{Fe} + \Delta l^{in}_{Fe}(t))\sqrt{2m\Delta E}}{\hbar}\right) \quad (27)$$

where $\Delta l^{in}_{Fe}(t)$ is the thickness increase of the inner SEI layer on the Fe surface [m], l^0_{Fe} is the initial thickness of the inner SEI layer on Fe and u_e is the Fermi velocity of electrons in metallic Fe [m·s^{-1}]. After proper derivation [6] Eq. (27) can be written as

$$\frac{dQ_{SEI,Fe}(t)}{dt} = \frac{F\rho_{Fe}u_e A_{Fe}}{M_{Fe}}P_0 \exp\left(-\frac{2\left(l^0_{Fe} + \frac{M_{Li}\delta_{Fe}Q_{SEI,Fe}(t)}{\rho^{in}A_{Fe}w^{in}_{Li}F}\right)\sqrt{2m\Delta E}}{\hbar}\right) \quad (28)$$

where δ_{Fe} is the ratio between the capacity losses due to the inner SEI

Table 1
Experimental conditions of the cycling experiments of A123 batteries.

	Temperature			Duration of each cycle (hours)
	20 °C	40 °C	60 °C	
Current (C-rate)	0.1	0.1	0.1	22.6–19.3
	0.5	0.5	0.5	5.5–4.8
	1.0	1.0	1.0	2.3–2.2
	2.0	2.0	2.0	2.1–1.8

and the total SEI on Fe. Replacing A_{Fe} in Eq. (28) using Eq. (26), yields

$$\frac{dQ_{SEI,Fe}(t)}{dt} = \frac{2\pi F\rho_{Fe}u_e N}{M_{Fe}}\left(\frac{3k_e c_{H^+}^2 M_{Fe} t}{2\pi N\rho_{Fe}}\right)^{2/3} P_0 \exp\left(-2\left(l_{Fe}^0 + \frac{M_{Li}\delta_{Fe}Q_{SEI,Fe}(t)}{2\pi N\rho^{in}w_{Li}^{in}F\left(\frac{3k_e c_{H^+}^2 M_{Fe} t}{2\pi N\rho_{Fe}}\right)^{2/3}}\right)\frac{\sqrt{2m\Delta E}}{\hbar}\right) \quad (29)$$

2.3. Summary of the proposed aging model

The total irreversible capacity losses upon storage ($\Delta Q_{ir}^{st}(t)$) at any time t can be written as

$$\Delta Q_{ir}^{st}(t) = Q_{SEI}^{st}(t) + Q_{Li,Fe}(t) + Q_{SEI,Fe}(t) \quad (30)$$

The maximum capacity of the battery ($Q_{max}^{st}(t)$) can then be represented by

$$\begin{aligned} Q_{\max}^{st}(t) &= Q_{\max}^{0} - \Delta Q_{ir}^{st}(t) \\ &= Q_{\max}^{0} - Q_{SEI}^{st}(t) - Q_{Li,Fe}(t) - Q_{SEI,Fe}(t) \end{aligned} \quad (31)$$

The total irreversible capacity loss during cycling ($\Delta Q_{ir}^{cy}(t)$) can be described by

$$\Delta Q_{ir}^{cy}(t) = Q_{SEI}^{\text{cov}}(t) + nQ_{SEI}^{fr} + Q_{Li,Fe}(t) + Q_{SEI,Fe}(t) \quad (32)$$

Consequently, the maximum capacity of the battery ($Q_{mx}^{cy}(t)$) is given by

$$\begin{aligned} Q_{\max}^{cy}(t) &= Q_{\max}^{0} - \Delta Q_{ir}^{cy}(t) \\ &= Q_{\max}^{0} - Q_{SEI}^{\text{cov}}(t) - nQ_{SEI}^{fr} - Q_{Li,Fe}(t) - Q_{SEI,Fe}(t) \end{aligned} \quad (33)$$

3. Experimental

3.1. Storage experiments

Commercially available LFP batteries (A123) were activated for 5 cycles at room temperature prior to conducting storage experiments. Subsequently, characterization cycles were performed at 20, 40 and 60 °C. To determine the EMF from the characterization cycles all batteries were charged in a constant-current constant-voltage (CCCV) mode. In the CC mode 1C charging rate was applied and the batteries were continuously charged in the CV-mode at 3.6 V for 2 h. In the subsequent cycles the batteries were discharged at the following constant currents: 0.1, 0.2, 0.3, 0.5, 0.75, 1, 1.5 and 2C-rate, with a cut-off voltage of 1.6 V. The measured voltage discharge curves were used to determine the EMF by regression extrapolation towards zero current. The extrapolation methods have been described in detail in Refs. [2,7,9,42–44].

After completing the characterization process all batteries were charged at 1C rate to various specified levels of SoC (namely 10, 50 and 100%). The corresponding charge capacities are denoted as Q_{ch}^{i}. After one month of storage batteries were discharged with the same current and cut-off voltage. The resulting discharge capacities are denoted as Q_{d}^{i}. This re-characterization was systematically carried out at the beginning of a new storage period. At the end of characterization process the batteries were charged again to the previous discharging capacity, *i.e.* $Q_{ch}^{i+1} = Q_{d}^{i}$, to keep intact the amount of charge from the previous storage period.

3.2. Cycling experiments

Similar to the storage experiments, commercially available LFP batteries (A123) were subject to 5 activation cycles at room temperature prior to conducting storage experiments. The characterizations were made at 20, 40 and 60 °C to obtain EMF curves. The characterization procedure was the same as used for the storage experiments (Section 3.1). After completing the characterization procedure all batteries were cycled under various conditions summarized in Table 1. The various cycling currents are given in the second column. The last column shows the duration of each cycle. Since the cycling currents are different, the duration of each cycle is also changing. One can see that actual duration of each cycle is slightly changing due to decreasing battery storage capacities. Regular re-characterization was applied for all batteries after approximately every 20 days.

Table 2
Model parameters of LFP batteries stored under various SoC and temperature conditions.

	Calendar aging								
	20 °C			40 °C			60 °C		
	10%	50%	100%	10%	50%	100%	10%	50%	100%
l_0^{in}/nm	2.54	2.54	2.54	2.54	2.54	2.54	2.54	2.54	2.54
$\frac{A_{C_6}}{m^2}$	23.69	23.69	23.69	23.69	23.69	23.69	23.69	23.69	23.69
$\frac{\Delta E}{eV}$	2.90	2.84	2.80	2.90	2.84	2.80	2.90	2.84	2.80
$\frac{Q_0}{AH}$	2.65	2.58	2.61	2.62	2.65	2.65	2.53	2.57	2.61
δ_{C_6}	$2.58{\cdot}10^{-2}$	$2.58{\cdot}10^{-2}$	$2.58{\cdot}10^{-2}$	$9.3{\cdot}10^{-3}$	$9.3{\cdot}10^{-3}$	$9.3{\cdot}10^{-3}$	$2.7{\cdot}10^{-3}$	$2.7{\cdot}10^{-3}$	$2.7{\cdot}10^{-3}$
$K_6/m^4(mol{\cdot}s)^{-1}$	$1.43{\cdot}10^{-21}$	$1.43{\cdot}10^{-21}$	$1.43{\cdot}10^{-21}$	$4.52{\cdot}10^{-18}$	$4.52{\cdot}10^{-18}$	$4.52{\cdot}10^{-18}$	$5.43{\cdot}10^{-15}$	$5.43{\cdot}10^{-15}$	$5.43{\cdot}10^{-15}$
$K_e^0/m^4(mol{\cdot}s)^{-1}$	$8.39{\cdot}10^{33}$	$8.39{\cdot}10^{33}$	$8.39{\cdot}10^{33}$	$8.39{\cdot}10^{33}$	$8.39{\cdot}10^{33}$	$8.39{\cdot}10^{33}$	$8.39{\cdot}10^{33}$	$8.39{\cdot}10^{33}$	$8.39{\cdot}10^{33}$
$E_a^0/J{\cdot}mol^{-1}$	$3.07{\cdot}10^{5}$	$3.07{\cdot}10^{5}$	$3.07{\cdot}10^{5}$	$3.07{\cdot}10^{5}$	$3.07{\cdot}10^{5}$	$3.07{\cdot}10^{5}$	$3.07{\cdot}10^{5}$	$3.07{\cdot}10^{5}$	$3.07{\cdot}10^{5}$
N	–	–	–	–	–	–	$1.0{\cdot}10^{6}$	$1.0{\cdot}10^{6}$	$1.0{\cdot}10^{6}$
δ_{Fe}	–	–	–	–	–	–	$1.0{\cdot}10^{-12}$	$1.0{\cdot}10^{-12}$	$1.0{\cdot}10^{-12}$
l_{Fe}^0/nm	–	–	–	–	–	–	241	241	241
A_{Fe}^0/m^2	–	–	–	–	–	–	$2.82{\cdot}10^{-5}$	$2.82{\cdot}10^{-5}$	$2.82{\cdot}10^{-5}$

Table 3
Model parameters of LFP batteries during cycling at various currents and temperatures.

	Cycling aging											
	20 °C				40 °C				60 °C			
	0.1C	0.5C	1C	2C	0.1C	0.5C	1C	2C	0.1C	0.5C	1C	2C
l_0^{in}/nm	2.54	2.54	2.54	2.54	2.54	2.54	2.54	2.54	2.54	2.54	2.54	2.54
$\frac{A_{C_6}}{m^2}$	23.69	23.69	23.69	23.69	23.69	23.69	23.69	23.69	23.69	23.69	23.69	23.69
$\frac{\Delta E}{eV}$	2.83	2.81	2.78	2.74	2.83	2.81	2.78	2.74	2.83	2.81	2.78	2.74
$\frac{Q_0}{AH}$	2.62	2.67	2.64	2.63	2.67	2.67	2.69	2.66	2.58	2.58	2.61	2.66
$\frac{Q_{SEI}^{fr}}{Ah}$	$4.77{\cdot}10^{-5}$	$4.77{\cdot}10^{-5}$	$4.77{\cdot}10^{-5}$	$4.77{\cdot}10^{-5}$	$8.32{\cdot}10^{-5}$	$8.32{\cdot}10^{-5}$	$8.32{\cdot}10^{-5}$	$8.32{\cdot}10^{-5}$	$1.39{\cdot}10^{-4}$	$1.39{\cdot}10^{-4}$	$1.39{\cdot}10^{-4}$	$1.39{\cdot}10^{-4}$
δ_{C_6}	$2.58{\cdot}10^{-2}$	$2.58{\cdot}10^{-2}$	$2.58{\cdot}10^{-2}$	$2.58{\cdot}10^{-2}$	$9.3{\cdot}10^{-3}$	$9.3{\cdot}10^{-3}$	$9.3{\cdot}10^{-3}$	$9.3{\cdot}10^{-3}$	$2.7{\cdot}10^{-3}$	$2.7{\cdot}10^{-3}$	$2.7{\cdot}10^{-3}$	$2.7{\cdot}10^{-3}$
$K_6/m^4(mol{\cdot}s)^{-1}$	$1.43{\cdot}10^{-21}$	$1.43{\cdot}10^{-21}$	$1.43{\cdot}10^{-21}$	$1.43{\cdot}10^{-21}$	$4.52{\cdot}10^{-18}$	$4.52{\cdot}10^{-18}$	$4.52{\cdot}10^{-18}$	$4.52{\cdot}10^{-18}$	$5.43{\cdot}10^{-15}$	$5.43{\cdot}10^{-15}$	$5.43{\cdot}10^{-15}$	$5.43{\cdot}10^{-15}$
$K_e^0/m^4(mol{\cdot}s)^{-1}$	$8.39{\cdot}10^{33}$	$8.39{\cdot}10^{33}$	$8.39{\cdot}10^{33}$	$8.39{\cdot}10^{33}$	$8.39{\cdot}10^{33}$	$8.39{\cdot}10^{33}$	$8.39{\cdot}10^{33}$	$8.39{\cdot}10^{33}$	$8.39{\cdot}10^{33}$	$8.39{\cdot}10^{33}$	$8.39{\cdot}10^{33}$	$8.39{\cdot}10^{33}$
$E_a^0/J{\cdot}mol^{-1}$	$3.07{\cdot}10^{5}$	$3.07{\cdot}10^{5}$	$3.07{\cdot}10^{5}$	$3.07{\cdot}10^{5}$	$3.07{\cdot}10^{5}$	$3.07{\cdot}10^{5}$	$3.07{\cdot}10^{5}$	$3.07{\cdot}10^{5}$	$3.07{\cdot}10^{5}$	$3.07{\cdot}10^{5}$	$3.07{\cdot}10^{5}$	$3.07{\cdot}10^{5}$
N	–	–						–	$1.0{\cdot}10^{6}$	$1.0{\cdot}10^{6}$	$1.0{\cdot}10^{6}$	$1.0{\cdot}10^{6}$
δ_{Fe}	–	–	–	–	–	–	–	–	$1.0{\cdot}10^{-12}$	$1.0{\cdot}10^{-12}$	$1.0{\cdot}10^{-12}$	$1.0{\cdot}10^{-12}$
l_{Fe}^0/nm	–	–	–	–	–	–	–	–	2.41	2.41	2.41	2.41
A_{Fe}^0/m^2	–	–	–	–	–	–	–	–	$2.82{\cdot}10^{-5}$	$2.82{\cdot}10^{-5}$	$2.82{\cdot}10^{-5}$	$2.82{\cdot}10^{-5}$

3.3. Inductively coupled plasma (ICP) spectrometry

In order to quantitatively determine the Fe deposition on graphite electrodes, graphite electrodes have been dismantled from both pristine and stored batteries. The battery storage condition was SoC = 10% at 60 °C for 7000 h. The dismantled graphite electrodes were cut into small pieces of 2.9×2 cm and immersed into 20 ml of 1 Molar H_2SO_4 (99.999%, Aldrich). The samples were stored at room temperature for 10 days to completely dissolve Fe from the graphite. The ICP measurements were carried out using standard calibration solutions.

4. Results and discussion

The maximum capacities upon storage $Q_{max}^{st}(t)$ and cycling $Q_{max}^{cy}(t)$ have been theoretically simulated by the above model. A Nonlinear Least Square (NLS) method was applied to estimate the unknown parameters of the model. Corresponding software was implemented in Matlab (R2017a). Parameters in the model under various ageing conditions are optimized simultaneously. The optimized parameters for storage and cycling are listed in Tables 2 and 3, respectively.

Fig. 2 shows the development of the experimental (symbols) and simulated (lines) Q_{max}^{st}/Q_{max}^{0} and Q_{max}^{cy}/Q_{max}^{0} values as a function of time at specified storage SoC, temperatures and cycling currents. In all cases the modeling results are in good agreement with the experimental data. Obviously, degradation at low temperatures is significantly smaller than that at higher temperatures, indicating a strong temperature dependence of degradation under both storage and cycling conditions. The influence of the SoC upon storage is shown in Fig. 2a–c. It can be seen that the capacity loss at low SoC is somewhat smaller than that at high SoC at all temperatures. Apart from the temperature, the (dis) charge current also plays an important role in the degradation. Fig. 2d–f shows that Q_{max}^{cy}/Q_{max}^{0} decays faster at higher currents.

Comparing Fig. 2a–c with Fig. 2d–f it is obvious that Q_{max}^{cy}/Q_{max}^{0} decreases faster during cycling than Q_{max}^{st}/Q_{max}^{0}during storage under all

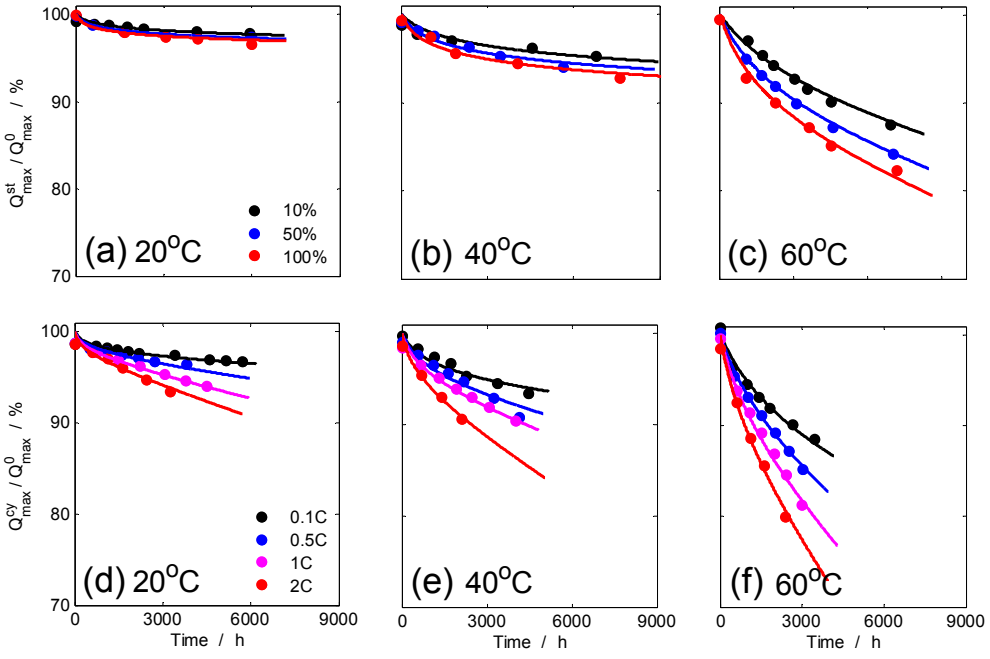

Fig. 2. Experimental (symbols) and simulated (lines) capacity development of cylindrical 2.3 Ah LFP batteries upon storage at various SoC (a–c) and cycling with various (dis)charge currents (d–f) at 20 °C, 40 °C and 60 °C.

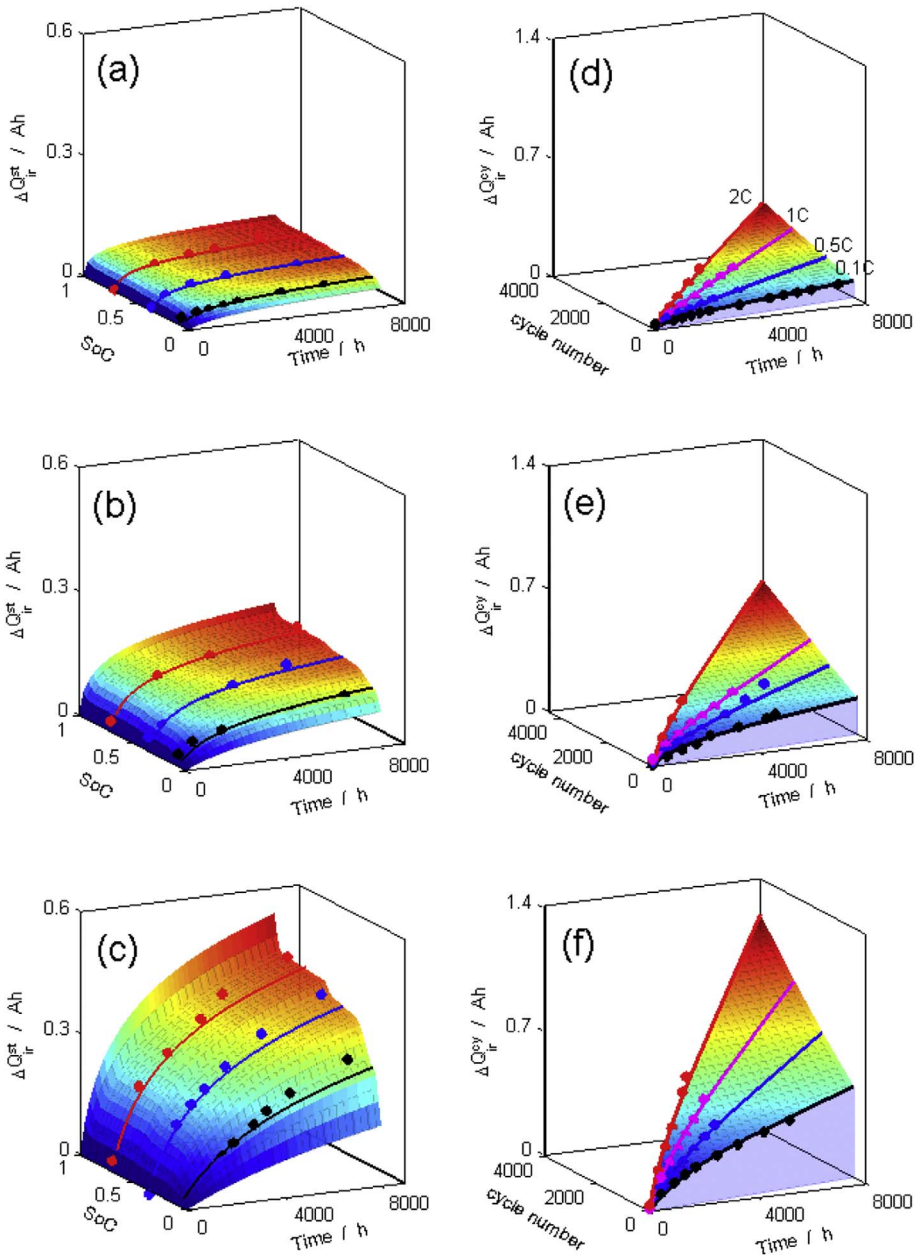

Fig. 3. Three-dimensional representation of simulated (lines) and experimental (symbols) capacity loss upon storage (ΔQ_{ir}^{st}) as a function of SoC and time (a–c) and cycling (ΔQ_{ir}^{cy}) as a function of cycle number and time (d–f) at 20 °C, 40 °C and 60 °C.

conditions. The volumetric changes of the graphite particles during cycling are the main reason causing this higher degradation. Cracks generated in the SEI layers will induce new SEI formation, leading to higher capacity losses during cycling compared to storage. Furthermore, as can be seen from Tables 2 and 3, the tunneling barrier (ΔE) during cycling is always smaller than during storage due to the overpotentials, which explains the higher degradation rate during cycling.

ΔQ_{ir}^{st} at various storage temperatures has been simulated according to Eq. (30) as a function of SoC and time. Both the simulations (lines) and experimental results (symbols) are plotted in Fig. 3a–c. Good agreement between the simulated and experimental results is found. ΔQ_{ir}^{st} becomes larger when SoC and time increase. The impact of SoC is more pronounced at elevated temperatures. The impact of temperature on ΔQ_{ir}^{st} is, however, more substantial than SoC. It should be noted that the SoC shown in Fig. 3a–c refers to that of the graphite electrode, which is different from that of the battery.

Fig. 3d–f shows the experimental and simulated irreversible capacity loss under various cycling temperature and current conditions as a function of time and cycle number. The simulation results are again in good agreement with the experimental results. Due to the volumetric changes of the graphite electrode, the SEI formation during cycling has been classified into two cases. As indicated in Fig. 1b, one process is the SEI formation on the covered surface area (A^{cov}), denoted as Q_{SEI}^{cov}, which obviously is time-dependent and has been described by Eq. (4). The other process is the SEI formation on the freshly formed surface area (A^{fr}) caused by the crack formation, denoted as Q_{SEI}^{cr}, which is cycle-number dependent and has been described by Eq. (7). When n is fixed, the cycling time t increases with decreasing (dis)charge current. Therefore both Q_{SEI}^{cov} and ΔQ_{ir}^{cy} increases with decreasing cycling current. When the cycle time t is fixed, the cycle number n increases with increasing (dis)charge current. Therefore both Q_{SEI}^{cr} and ΔQ_{ir}^{cy} increases with increasing cycling current.

In order to get information about the individual contributions of time and SoC on the degradation process, the capacity loss is plotted as a function of time and SoC. Fig. 4a–c shows the development of the simulated (lines) and experimental (symbols) irreversible capacity loss as a function of storage time at various storage SoC and temperatures. As can be concluded from Eqs. ((3), (21), (29) and (30), ΔQ_{ir}^{st} increases

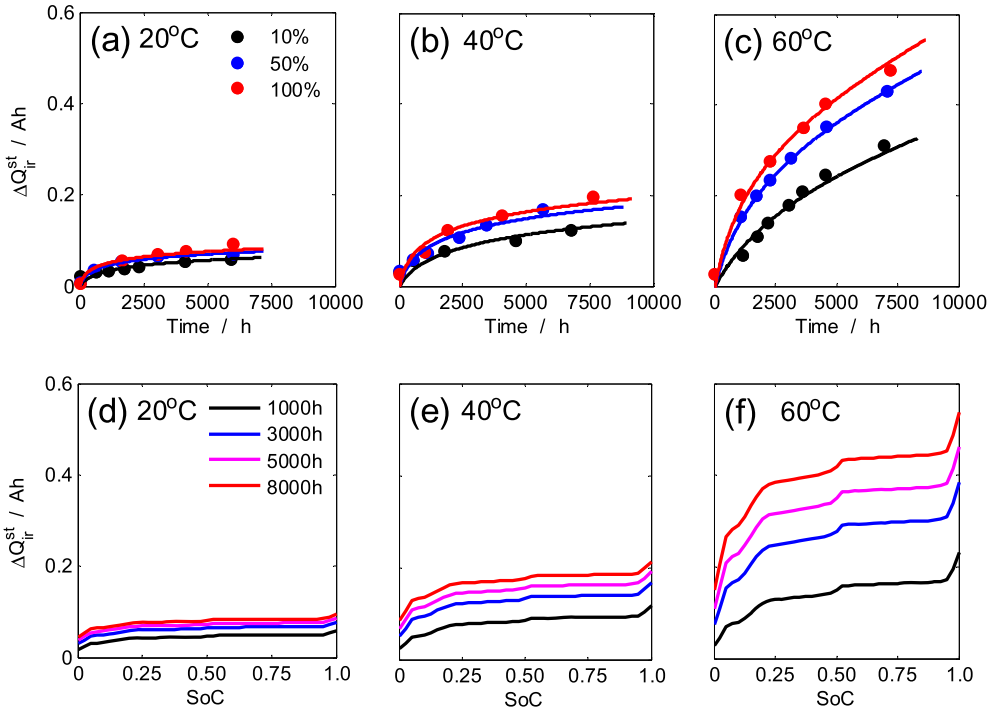

Fig. 4. Irreversible capacity loss (ΔQ_{ir}^{st}) of LFP batteries as a function of storage time (a–c) at various indicated SoC and as a function of SoC (d–f) at various storage times at 20 °C, 40 °C and 60 °C.

logarithmically with time. Fig. 4d–f shows the development of ΔQ_{ir}^{st} as a function of SoC at various storage times and temperatures. Interestingly, ΔQ_{ir}^{st} increases with increasing SoC and the trend closely follows the anode voltage plateau development. This is because the SEI formation rate is dependent on the electron tunneling barrier ΔE, which is a function of the graphite electrode Fermi level (E_f), according to $\Delta E = U - E_f$. Furthermore, E_f is a function of the graphite Electro-Motive Force (EMF) described by $E_f(x) = E_f(LiC_6) - e(\varphi_{Li_xC_6} - \varphi_{LiC_6})$. Obviously, the electrode potential at various SoC follows condition $\varphi_{100\%} < \varphi_{50\%} < \varphi_{10\%}$, indicating that the electrode Fermi level at various SoC follows $E_f(100\%) > E_f(50\%) > E_f(10\%)$ and $\Delta E(100\%) < \Delta E(50\%) < \Delta E(10\%)$. Therefore, the capacity fade develops as a function of the SoC of the negative electrode: the lower the negative electrode SoC, the higher ΔQ_{ir}^{st} is.

The dependence of current density j_{SEI} on both current and temperature is illustrated in Fig. 5. The values of j_{SEI} has been calculated at 4 different cycling times: 1000 (black), 2000 (blue), 3000 (pink) and 4000 h (red) at various currents at 60 °C are plotted as a function of $\sqrt{\Delta E}$ and T^{-1}, respectively. It can be seen that j_{SEI} increases with increasing current and temperature. Obviously, a linear relationship between $\ln j_{SEI}$ and $\sqrt{\Delta E}$, T^{-1} can be observed at various cycling time t, indicating that j_{SEI} follows an Arrhenius-type of dependence on $\sqrt{\Delta E}$ and T^{-1}.

At low and moderate temperatures the irreversible capacity losses are mainly caused by Li^+ immobilization in the SEI formation. However, the contribution of cathode dissolution on the capacity loss becomes significant at elevated temperatures. The origin of the cathode dissolution has been related to the proton exchange reaction, described by Eqs. (10) and (11). The proton concentration in the electrolyte is essential for Fe^{2+} ions dissolution. Fe^{2+} ions will be reduced at the anode. The Fe dissolution flux and the subsequent reduction flux are described by Eq. (17). The optimized exchange constant k_e in Tables 2 and 3 is clearly found to be temperature-dependent.

According to Eq. (18), the total amount of Fe deposited on the graphite electrode (N_{Fe}), depends on time, H^+ concentration and rate constant k_e. Since this constant always enter the formulas in combination with $c_{H^+}^2$ it cannot be separately identified. However, it has been reported by many battery manufacturers that c_{H^+} generally is of the order of 10 ppm [45]. In order to validate Eq. (18), ICP measurements on "dissolved" graphite electrodes have been carried out. No iron has been detected in pristine graphite. However, considerable amount of iron is found in stored graphite electrodes. It has, for example, been analyzed that the amount of Fe, deposited on the graphite electrode, is approximately 0.1 mmol after 7000 h of storage, in good agreement with simulation results produced Eq. (18).

Fig. 6a shows the simulated development of the surface area of the precipitated Fe particles (A_{Fe}) at the graphite electrode as a function of time. It can be seen from Eq. (26) that A_{Fe} is determined by the temperature-dependent k_e and by c_{H^+}. Therefore, A_{Fe} is only determined by the ambient temperature and the H^+ concentration in the electrolyte and is therefore independent on the testing conditions, such as SoC and current. The SEI formation on these Fe particles is also assumed to be determined by electron tunneling. However, the thickness of the inner SEI layer on the Fe surface is found to be thinner than the corresponding layer on the graphite electrode. Therefore, the SEI formation rate on the Fe surface is larger than that at the graphite electrode. Fig. 6b and c shows the evolution of $Q_{SEI,Fe}$ as a function of time at various SoC and cycling currents at 60 °C. $Q_{SEI,Fe}$ increases with increasing SoC and (dis)charge currents since the electron tunneling barrier on the Fe surface is smaller at higher SoC and current.

Fig. 7a–c shows the simulated inner SEI layer growth upon storage at the various indicated SoC and temperatures. Edström et al. [14], experimentally studied the thickness of inner SEI layer using X-ray photoelectron spectroscopy (XPS) and found it to be approximately 20 Å. These experimental results are in good agreement with the simulated SEI inner layer thickness in the present model. It is commonly accepted that electrode potential has a significant influence on the SEI formation products [15]. Fig. 7a–c shows that the inner SEI layer grows faster at high SoC at all temperatures. Moreover, the inner SEI layer grows faster at lower temperatures. According to the definition of δ_{C_6}, the growth of inner SEI layer is proportional to the product of δ_{C_6} and the total irreversible capacity losses [6]. The temperature influence on the inner SEI layer growth can be explained by the temperature dependence of δ_{C_6} as shown in Table 2, while the different growth rates at various SoC are attributed to the different tunneling barriers.

The growth of the outer SEI layer under various storage conditions is shown in Fig. 7d–f. It shows a similar trend as found for the SEI inner layer but at considerably higher rates. At 20 °C, the outer SEI layer

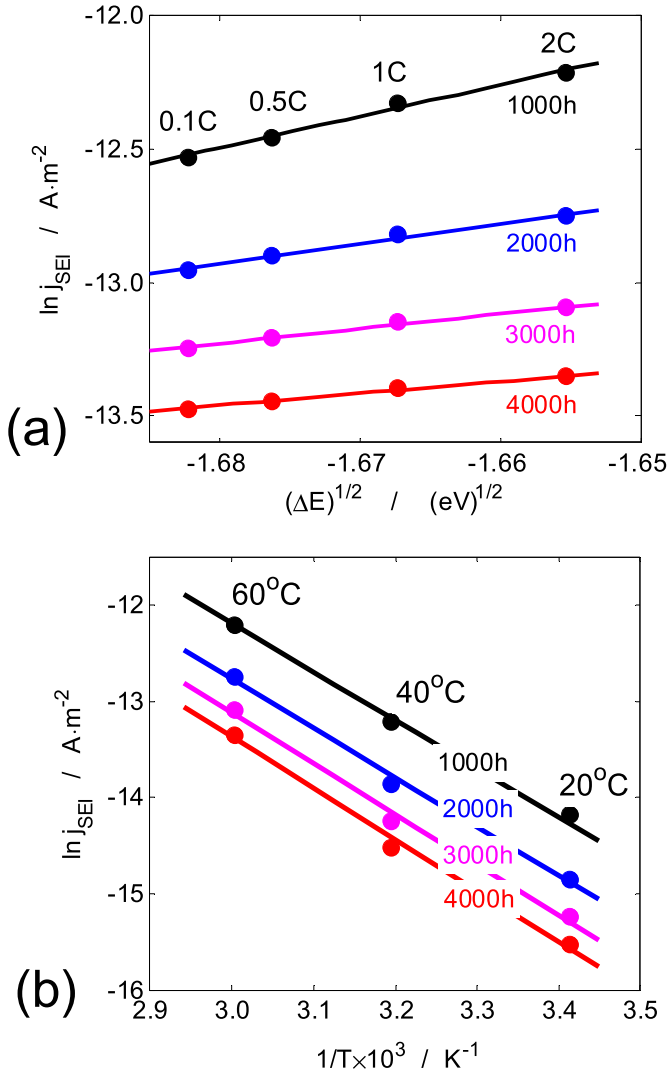

Fig. 5. Development of $\ln j_{SEI}$ as a function of (a) energy barrier ($\sqrt{\Delta E}$) and (b) temperature at 4 different cycling times: 1000 (black), 2000 (blue), 3000 (pink) and 4000 h (red). (For interpretation of the references to colour in this figure legend, the reader is referred to the web version of this article.)

increased with about 15 nm after 9000 h storage (Fig. 7d), while this amounts to, for example, ~75 nm at 60 °C at 100% SoC (Fig. 7f). The influence of SoC on the outer SEI layer growth is minor at 20 °C but becomes more significant at 60 °C. The increase of the outer SEI layer is about 45 nm when stored at 10% SoC while is 75 nm at 100% SoC at 60 °C. Interestingly, it is found that the growth of the inner SEI layer at higher temperatures is slower than that at lower temperatures while the opposite holds for the outer SEI layer.

Fig. 8a–c shows the simulated increase of the SEI inner layer thickness upon cycling at 0.1, 0.5, 1 and 2 C-rate at 20 °C, 40 °C and 60 °C. It is found that the inner SEI layer grows somewhat faster at higher currents for all temperatures. The influence of temperature on the inner SEI growth rate can be explained by the temperature dependence of δ_{C_6} (see Table 3). The growth of the outer SEI layer under cycling conditions is shown in Fig. 8d–f. It reveals a similar growth trend as found in Fig. 7d–f. The temperature has a considerable impact on the growth rate of the outer SEI layer. The influence of the current is, however, minor at 20 °C but becomes significant at 60 °C.

Experimental investigations of the outer SEI layer thickness is difficult due to its porous and fragile structure. Before conducting SEI characterization, the graphite electrode is usually rinsed to remove the crystalized Li salt from the electrolyte. However, it has also been reported that the outer SEI layers can be partially dissolved in the electrolyte/solvent, which makes these investigations quite inaccurate. The simulations, based on the presented SEI models, provide now an efficient way to accurately estimate the growth of both the inner and outer SEI layers.

According to Eqs. (3) and (4) the formation rate of SEI is determined by the State-of-Charge, the energy barrier ΔE, the inner layer thickness and the surface area. For batteries produced in the same batch, the surface area and initial SEI inner layer thickness should be similar. So, the State-of-Charge and energy barrier ΔE are the most important factors, controlling the formation rate of SEI for a particular batch. Tables 2 and 3 give a summary of all discussed parameters.

5. Conclusions

A comprehensive electron-tunneling-based model for lithium immobilization is developed to accurately describe the ageing of C_6/$LiFePO_4$ (LFP) batteries. This model includes a temperature-dependent cathode dissolution process and can describe the capacity losses of LFP batteries in very much detail under a wide range of storage and cycling conditions.

The SEI formation model presumes the existence of a porous outer and dense inner SEI layers. Electron tunneling through the inner SEI layer is considered to be the rate-determined step in the SEI formation process. Both SEI layers are formed at the interface between the inner and outer SEI layers. The outer SEI layer grows much faster than the inner layer. The initial thickness of the inner layer achieved after activation process will, to a large degree, determine the subsequent degradation rate.

The capacity losses at moderate aging temperatures are all attributed to the immobilization of Li-ions in the SEI layers. It has been concluded that the capacity losses are strongly dependent on the storage SoC and the cycling current. The capacity losses during cycling are larger than during storage at the same operation time due to the additional crack formation upon (dis)charging. These cracks generate free graphite surface areas exposed to the electrolyte, where new SEI will be easily formed. The capacity losses due to the SEI formation on these newly formed graphite surfaces are a function of both the cycling

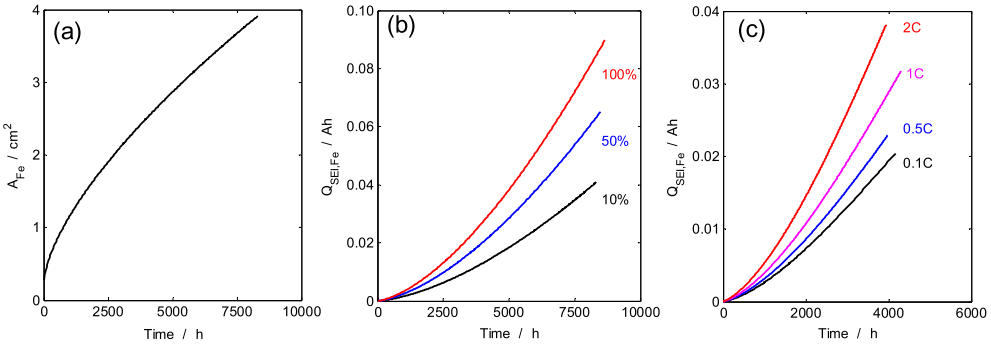

Fig. 6. The development of the surface area of precipitated Fe particles on the graphite electrode (a) and the capacity loss ($Q_{SEI,Fe}$) caused by the SEI formation onto the Fe surface at the various indicated SoC upon storage (b) and various currents (c) upon cycling at 60 °C.

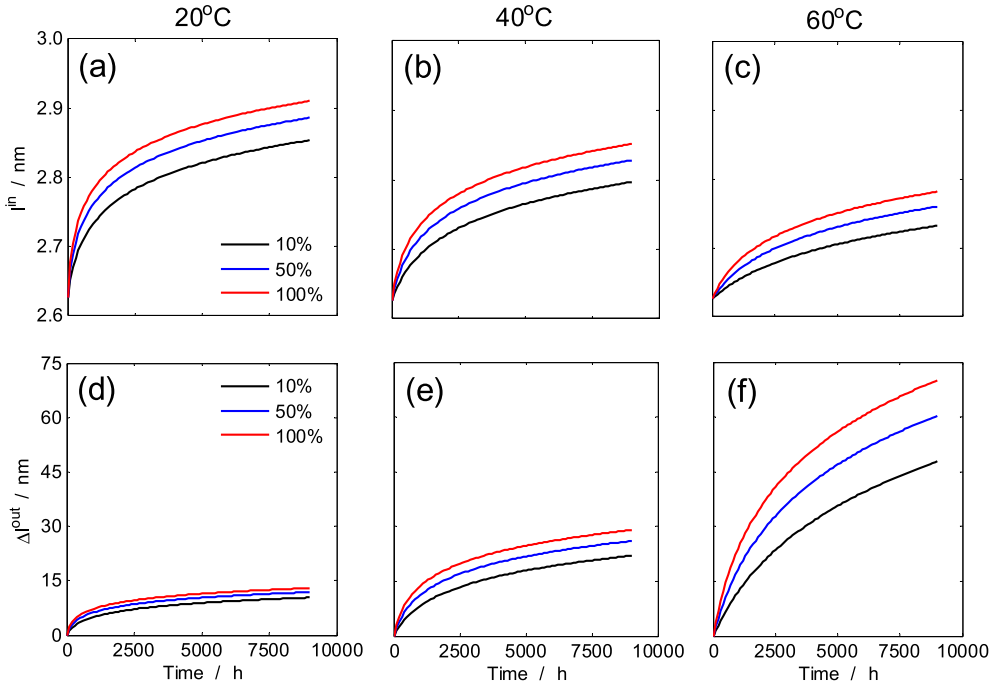

Fig. 7. The development of the inner (a–c) and outer (d–f) SEI layers upon storage at various indicated SoC at 20 °C (a), 40 °C (b) and 60 °C (c).

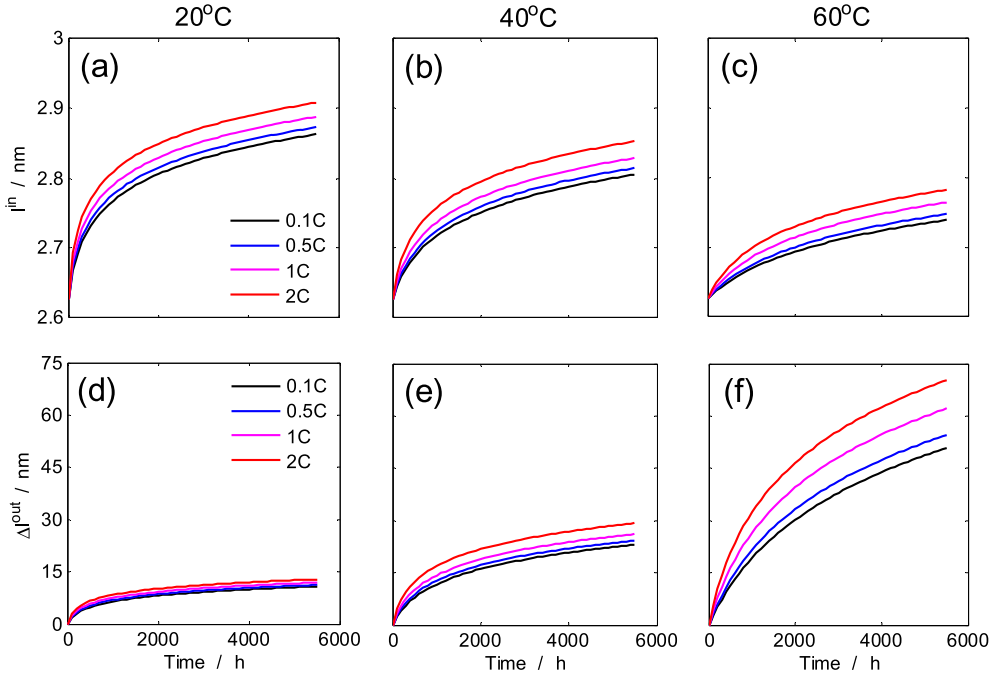

Fig. 8. The development of the outer SEI layer upon cycling at various currents and SoC at 20 °C (a), 40 °C (b) and 60 °C (c).

number and charging time. Nearly a logarithmical relation between the capacity loss and calendar aging time was observed.

A cathode dissolution model is used to describe the transition-metal dissolution process from the cathode at the elevated temperatures under both storage and cycling conditions. Cathode dissolution is assumed to be initiated by a proton-exchange reaction. The concentration of protons in the electrolyte ultimately determines the cathode dissolution rate. The dissolved metal ions can be transported to the anode and reduced at the graphite surface. Both cathode dissolution and metal deposition will induce higher capacity losses. The SEI formation on these metal-cluster surfaces has also been simulated and the simulations are in good agreement with the experimental results.

List of symbols.

Symbol	Meaning	Value	Unit
A	Surface area of the graphite electrode		m^2
A^{cov}	SEI covered surface areas of C_6 electrode		m^2
A^{fr}	Fresh surface areas of C_6 electrode		m^2
A_{Fe}	Total surface areas of Fe particles on the graphite electrode		m^2

A_{LiFePO_4}	Total surface areas of $LiFePO_4$ electrode		m^2
$C_{Fe^{2+}}(t)$	Fe^{2+} concentration in the electrolyte at time^t		$mol{\cdot}L^{-1}$
$C_{H^+}(t)$	H^+ concentration in the electrolyte at time^t		$mol{\cdot}L^{-1}$
$C_{LiFePO_4}(t)$	Surface concentration of $LiFePO_4$		$mol{\cdot}L^{-2}$
$E_f(x)$	Fermi level of Li_xC_6 electrode		eV
$E_f(LiC_6)$	Fermi level of LiC_6 electrode		eV
E_a^e	Activation energy for cathode dissolution		$J{\cdot}mol^{-1}$
ΔE	Energy barrier for electron tunneling		eV
e	Charge of single electron	$1.6{\cdot}10^{-19}$	C
F	Faraday constant	96485	$C{\cdot}mol^{-1}$
$J^a_{Fe^{2+}}$	Total reduction flux of Fe^{2+} at the anode		$mol{\cdot}s^{-1}$
$J^c_{Fe^{2+}}$	Total dissolution flux of Fe^{2+} from the cathode		$mol{\cdot}s^{-1}$
J_{SEI}	Current density of SEI formation		$A{\cdot}m^{-2}$
$\widetilde{K}_d$	Dissociation reaction constant of LiH_2PO_4	depends on parameter	
K_e	Combined exchange reaction constant	depends on parameter	
K_e^0	Pre-exponential factor	depends on parameter	
$\widetilde{K}_e$	Exchange reaction constant	depends on parameter	
K_p	Deposition reaction constant of Fe^{2+} on graphite	depends on parameter	
l^{in}	Thickness of the inner SEI layer on C_6		m
l_0^{in}	Initial thickness of the inner SEI layer on C_6		m
l_{Fe}^0	Initial thickness of the inner SEI on Fe		m
M_{C_6}	Mole mass of graphite	72.06	$g{\cdot}mol^{-1}$
M_{Fe}	Mole mass of Fe	55.85	$g{\cdot}mol^{-1}$
M_{Li}	Mole mass of Lithium	6.94	$g{\cdot}mol^{-1}$
m	Electron mass	$9.11{\cdot}10^{-28}$	g
N	Total numbers of Fe particles		–
N_{Fe}	Total amount of Fe reduced on graphite		mol
P	Tunneling probability		–
P_0	Pre-exponential coefficient		–
Q^i_{ch}	Charge capacity in i^{th} cycle		Ah
Q^i_d	Discharge capacity in i^{th} cycle		Ah
$Q_{Li,Fe}$	Capacity loss caused by Fe dissolution and deposition		Ah
Q_{LiFePO_4}	Total capacity of the $LiFePO_4$ electrode		Ah
$Q^0_{LiFePO_4}$	Maximum $LiFePO_4$ electrode capacity (pristine state)		Ah
$Q_{\downarrow}\max{}^{\uparrow}0$	Maximum battery discharge capacity at $t = 0$		Ah
$Q_{\downarrow}\max{}^{\uparrow}t$	Maximum battery discharge capacity at time^t		Ah
$Q^{cy}_{\max(t)}$	Maximum discharge capacity at time^t during cycling		Ah
$Q^{st}_{Max(T)}$	Maximum discharge capacity at time^t during storage		Ah
Q^{cov}_{SEI}	Capacity loss due to the SEI formation on A^{cov}		Ah
Q^{cr}_{SEI}	Accumulated capacity loss due to formation of SEI on A^{fr}	Ah	
Q^{cy}_{SEI}	Capacity loss caused by SEI formation during cycling		Ah
Q^{fr}_{SEI}	Capacity loss due to the SEI formation on A^{fr} in each cycle		Ah
Q^{st}_{SEI}	Capacity loss caused by SEI formation during storage		Ah
$Q_{SEI,Fe}$	Irreversible capacity losses caused by SEI formation on Fe		Ah
ΔQ^{cy}_{ir}	Total irreversible capacity loss induced by cycling aging		Ah
ΔQ^{st}_{ir}	Total irreversible capacity loss during storage		Ah
R	Gas constant	8.314	$J{\cdot}(mol{\cdot}K)^{-1}$
r	Average radius of Fe particles		m
T	Temperature		K
t	Time		s
u_e	Fermi velocity of electrons in bulk of metallic Fe		$m{\cdot}s^{-1}$
V_{Fe}	Volume of Fe particles		m^3
v_e	Electrons Fermi velocity in the bulk of graphite		$m{\cdot}s^{-1}$
W^{in}_{Li}	Average weight percentage of Li in the inner layer of SEI		–
x	State-of-Charge of the graphite electrode		–
δ_{C_6}	Capacity fraction between inner and total SEI layer on C_6		–
δ_{Fe}	Capacity fraction between inner and total SEI layer on Fe		–
$\varphi_{Li_xc_6}$	Electrode potential of Li_xC_6		V
φ_{Lic_6}	Electrode potential of LiC_6		V
χ	Capacity loss due to the SEI formation on A^{fr} in each cycle		Ah
ρ_{Fe}	Density of Fe	$7.86{\cdot}10^6$	$g{\cdot}m^{-3}$
ρ_{C_6}	Density of graphite	$2.266{\cdot}10^6$	$g{\cdot}m^{-3}$
ρ^{in}	Density of the inner SEI layer		$g{\cdot}m^{-3}$

Acknowledgements

The authors appreciate the financial support from the Horizon 2020 program of the European Union under the grant of the AutoDrive project 'Advancing fail-aware, fail-safe, and fail-operational electronic components, systems, and architectures for fully automated driving to make future mobility safer, affordable, and end-user acceptable' (Grant No. 737469) and the grant from the Science and Technology Office, Fujian Province (Grant No. 2014HZ0002-1).

References

[1] P.H.L. Notten, D.L. danilov, Adv. Chem. Eng. Sci. 4 (2014) 62–72.
[2] M.S. Rad, D.L. Danilov, M. Baghalha, M. Kazemeini, P.H.L. Notten, Electrochimica Acta 102 (2013) 183–195.
[3] P. Arora, R.E. White, M. Doyle, J. Electrochem. Soc. 145 (1998) 3647–3667.
[4] M. Kassem, J. Bernard, R. Revel, S. Pelissier, F. Duclaud, C. Delacourt, J. Power Sources 208 (2012) 296–305.
[5] D. Li, D. Danilov, Z. Zhang, H. Chen, Y. Yang, P.H.L. Notten, ECS Trans. 62 (8) (2014).
[6] D.J. Li, D. Danilov, Z.R. Zhang, H.X. Chen, Y. Yang, P.H.L. Notten, J. Electrochem. Soc. 162 (2015) A858–A869.
[7] D.J. Li, D.L. Danilov, L. Gao, Y. Yang, P.H.L. Notten, Electrochimica Acta 210 (2016) 445–455.
[8] D.J. Li, D.L. Danilov, L. Gao, Y. Yang, P.H.L. Notten, J. Electrochem. Soc. 163 (2016) A3016–A3021.
[9] D.J. Li, D.L. Danilov, J. Xie, L. Raijmakers, L. Gao, Y. Yang, P.H.L. Notten, Electrochimica Acta 190 (2016) 1124–1133.
[10] E. Peled, D. Golodnitsky, A. Ulus, V. Yufit, Electrochimica Acta 50 (2004) 391–395.

[11] D. Aurbach, J. Power Sources 89 (2000) 206–218.
[12] D. Aurbach, E. Zinigrad, Y. Cohen, H. Teller, Solid State Ionics 148 (2002) 405–416.
[13] K. Xu, Energies 3 (2010) 135–154.
[14] A.M. Andersson, M. Herstedt, A.G. Bishop, K. Edstrom, Electrochimica Acta 47 (2002) 1885–1898.
[15] S. Leroy, F. Blanchard, R. Dedryvere, H. Martinez, B. Carre, D. Lemordant, D. Gonbeau, Surf. Interface Analysis 37 (2005) 773–781.
[16] S.K. Jeong, M. Inaba, Y. Iriyama, T. Abe, Z. Ogumi, J. Power Sources 119 (2003) 555–560.
[17] J.T. Lee, N. Nitta, J. Benson, A. Magasinski, T.F. Fuller, G. Yushin, Carbon 52 (2013) 388–397.
[18] S. Leroy, H. Martinez, R. Dedryvere, D. Lemordant, D. Gonbeau, Appl. Surf. Sci. 253 (2007) 4895–4905.
[19] P. Verma, P. Maire, P. Novák, Electrochimica Acta 55 (2010) 6332–6341.
[20] K. Xu, A. von Cresce, J. Mater. Chem. 21 (2011) 9849–9864.
[21] J. Christensen, J. Newman, J. Electrochem. Soc. 151 (2004) A1977–A1988.
[22] P. Lu, S.J. Harris, Electrochem. Commun. 13 (2011) 1035–1037.
[23] E. Peled, D. Golodnitsky, G. Ardel, J. Electrochem. Soc. 144 (1997) L208–L210.
[24] E. Peled, J. Electrochem. Soc. 126 (1979) 2047–2051.
[25] J. Christensen, J. Newman, J. Electrochem. Soc. 152 (2005) A818.
[26] M. Onuki, S. Kinoshita, Y. Sakata, M. Yanagidate, Y. Otake, M. Ue, M. Deguchi, J. Electrochem. Soc. 155 (2008) A794.
[27] A.J. Smith, J.C. Burns, J.R. Dahn, Electrochem. Solid-State Lett. 13 (2010) A177.
[28] H.J. Ploehn, P. Ramadass, R.E. White, J. Electrochem. Soc. 151 (2004) A456–A462.
[29] J.L. Esbenshade, A.A. Gewirth, J. Electrochem. Soc. 161 (2014) A513–A518.
[30] Y.X. Lin, Z. Liu, K. Leung, L.Q. Chen, P. Lu, Y. Qi, J. Power Sources 309 (2016) 221–230.
[31] T. Baumhofer, M. Bruhl, S. Rothgang, D.U. Sauer, J. Power Sources 247 (2014) 332–338.
[32] K. Amine, J. Liu, I. Belharouak, Electrochem. Commun. 7 (2005) 669–673.
[33] H.C. Wu, C.Y. Su, D.T. Shieh, M.H. Yang, N.L. Wu, Electrochem. Solid State Lett. 9 (2006) A537–A541.
[34] M. Koltypin, D. Aurbach, L. Nazar, B. Ellis, Electrochem. Solid State Lett. 10 (2007) A40–A44.
[35] J.J. Wang, Y.J. Tang, J.L. Yang, R.Y. Li, G.X. Liang, X.L. Sun, J. Power Sources 238 (2013) 454–463.
[36] N.A.W. Holzwarth, S. Rabii, L.A. Girifalco, Phys. Rev. B 18 (1978) 5190–5205.
[37] N.A.W. Holzwarth, S. Rabii, Mater. Sci. Eng. 31 (1977) 195–200.
[38] G.K. Wertheim, P. Vanattekum, S. Basu, Solid State Commun. 33 (1980) 1127–1130.
[39] A.M. Andersson, A. Henningson, H. Siegbahn, U. Jansson, K. Edstrom, J. Power Sources 119 (2003) 522–527.
[40] M.B. Pinson, M.Z. Bazant, J. Electrochem. Soc. 160 (2013) A243–A250.
[41] R. Deshpande, M. Verbrugge, Y.T. Cheng, J. Wang, P. Liu, J. Electrochem. Soc. 159 (2012) A1730–A1738.
[42] V. Pop, H.J. Bergveld, J.H.G. Op het Veld, P.P.L. Regtien, D. Danilov, P.H.L. Notten, J. Electrochem. Soc. 153 (2006) A2013–A2022.
[43] D. Danilov, R.A.H. Niessen, P.H.L. Notten, J. Electrochem. Soc. 158 (2011) A215–A222.
[44] H.J. Bergveld, W.S. Kruijt, P.H.L. Notten, Battery Management Systems, Design by Modeling, Kluwer Academic Publishers, Boston, 2002.
[45] C. Herriot, Entegris INC, Printed in US, 9000–7333ENT-1212, (2012).